White light Sagnac interferometer for snapshot multispectral imaging

Michael W. Kudenov,[1] Matthew E. L. Jungwirth, [1] Eustace L. Dereniak, [1] and Grant R. Gerhart[2]

[1]College of Optical Science, The University of Arizona, 1630 E. University Blvd., Tucson, AZ 85721
[2]U.S. Army TACOM, 6501 E. 11 Miles Rd., Warren, MI 48397

Abstract: The theoretical and experimental demonstration of a multispectral Sagnac interferometer (MSI) is presented. The MSI was created by including two multiple-order blazed diffraction gratings in both arms of a standard polarization Sagnac interferometer (PSI). By introducing these high-order diffractive structures, unique spectral passbands can be amplitude modulated onto coincident carrier frequencies. Extraction of the modulated multispectral images, corresponding to each passband, is accomplished within the Fourier domain. This yields a unique multispectral sensor capable of imaging all the passbands in a single snapshot. First, the theoretical operating principles of a polarization Sagnac interferometer are discussed to provide a context for the MSI. This is followed by the theoretical and experimental development of the MSI, which is an extension of a dispersion-compensated polarization Sagnac interferometer (DCPSI) based polarimeter. Indoor and outdoor testing and validation of the MSI is performed by observing vegetation, demonstrating the ability of our experimental setup to detect four distinctive spectral passbands.

OCIS codes: (110.3175) Interferometric imaging; (300.6190) Spectrometers; (110.4234) Multispectral and hyperspectral imaging

References and links

1. C. M. Biradar, P. Thenkabail, A. Platonov, X. Xiao *et. al*. "Water productivity mapping methods using remote sensing," J. Appl. Remote Sens. **2**, 023544 (2008).
2. R. M. Levenson and J. R. Mansfield, "Multispectral Imaging in Biology and Medicine: Slices of Life," Cytometry Pt. A. **69A**, 748-758 (2006).
3. A. Vogel, V. Chernomordik, J. Riley, M. Hassan, F. Amyot *et. al*. "Using noninvasive multispectral imaging to quantitatively assess tissue vasculature," J. Biomed. Opt. **12** (5) 051604 (2007).
4. M. Kise, B. Park, K. C. Lawrence, W. R. Windham, "Compact Multi-spectral Imaging System for Contaminant Detection on Pultry Carcass," Proc. SPIE. **6503** 650305 (2007).
5. F. Sigernes, J. M. Holmes, M. Dyrland, D. A. Lorentzen, T. Svenoe, *et. al*. "Sensitivity calibration of digital colour cameras for auroral imaging," Opt. Express. **16** (20), 15623-15632 (2008).
6. G. Themelis, J. Yoo, V. Ntziachristos, "Multispectral imaging using multiple-bandpass filters," Opt. Lett. **33** (9), 1023-1025 (2008).
7. K. Oka, T. Kaneko, "Compact complete imaging polarimeter using birefringent wedge prisms," Opt. Express **11** (13) 1510-1519 (2003).
8. M. Kudenov, L. Pezzaniti, E. Dereniak, G. Gerhart, "Prismatic imaging polarimeter calibration for the infrared spectral region," Opt. Express. **16**, 13720-13737 (2008).
9. M. W. Kudenov, M. E. L. Jungwirth, E. L. Dereniak, and G. R. Gerhart, "White light Sagnac interferometer for snapshot polarimetric imaging," Opt. Express. (to be published).
10. R. Suda, N. Saito, and K. Oka, "Imaging Polarimetry by Use of Double Sagnac Interferometers," in Extended Abstracts of the 69th Autumn Meeting of the Japan Society of Applied Physics (Japan Society of Applied Physics, Tokyo, 2008), p. 877 (in Japanese).
11. H. Luo, K. Oka, E. DeHoog, M. Kudenov, J. Schiewgerling, and E. Dereniak, "Compact and miniature snapshot imaging polarimeter," Appl. Opt. **47** (24), 4413-4417 (2008).
12. Dennis Goldstein, *Polarized Light* (Marcel Dekker, 2003).
13. J. C. Wyant, "OTF measurements with a white light source: an interferometric technique," Appl. Opt. **14** (7), 1613-1615 (1975).

Report Documentation Page

Form Approved
OMB No. 0704-0188

1. REPORT DATE	2. REPORT TYPE	3. DATES COVERED
10 NOV 2009	**N/A**	**-**

4. TITLE AND SUBTITLE	5a. CONTRACT NUMBER
White light Sagnac interferometer for snapshot multispectral imaging (PREPRINT)	5b. GRANT NUMBER
	5c. PROGRAM ELEMENT NUMBER

6. AUTHOR(S)	5d. PROJECT NUMBER
Michael W. Kudenov; Matthew E. L. Jungwirth; Eustace L. Dereniak; Grant R. Gerhart;	5e. TASK NUMBER
	5f. WORK UNIT NUMBER

7. PERFORMING ORGANIZATION NAME(S) AND ADDRESS(ES)	8. PERFORMING ORGANIZATION REPORT NUMBER
1College of Optical Science, The University of Arizona, 1630 E. University Blvd., Tucson, AZ 85721 US Army RDECOM-TARDEC 6501 E 11 Mile Rd Warren, MI 48397-5000, USA	**20365RC**

9. SPONSORING/MONITORING AGENCY NAME(S) AND ADDRESS(ES)	10. SPONSOR/MONITOR'S ACRONYM(S)
US Army RDECOM-TARDEC 6501 E 11 Mile Rd Warren, MI 48397-5000, USA	**TACOM/TARDEC**
	11. SPONSOR/MONITOR'S REPORT NUMBER(S) **20365RC**

12. DISTRIBUTION/AVAILABILITY STATEMENT
Approved for public release, distribution unlimited

13. SUPPLEMENTARY NOTES
Submitted for publication in Optics Express Journal, The original document contains color images.

14. ABSTRACT
Abstract: The theoretical and experimental demonstration of a multispectral Sagnac interferometer (MSI) is presented. The MSI was created by including two multiple-order blazed diffraction gratings in both arms of a standard polarization Sagnac interferometer (PSI). By introducing these high-order diffractive structures, unique spectral passbands can be amplitude modulated onto coincident carrier frequencies. Extraction of the modulated multispectral images, corresponding to each passband, is accomplished within the Fourier domain. This yields a unique multispectral sensor capable of imaging all the passbands in a single snapshot. First, the theoretical operating principles of a polarization Sagnac interferometer are discussed to provide a context for the MSI. This is followed by the theoretical and experimental development of the MSI, which is an extension of a dispersion-compensated polarization Sagnac interferometer (DCPSI) based polarimeter. Indoor and outdoor testing and validation of the MSI is performed by observing vegetation, demonstrating the ability of our experimental setup to detect four distinctive spectral passbands. Ó2009 Optical Society of America

15. SUBJECT TERMS

16. SECURITY CLASSIFICATION OF:			17. LIMITATION OF ABSTRACT	18. NUMBER OF PAGES	19a. NAME OF RESPONSIBLE PERSON
a. REPORT	b. ABSTRACT	c. THIS PAGE			
unclassified	**unclassified**	**unclassified**	**SAR**	**15**	

14. J. W. Goodman, *Introduction to Fourier Optics* (Roberts & Company, 2005).
15. J. Craven, M. Kudenov, E. Dereniak, "False signature reduction in infrared channeled spectropolarimetry," Proc. SPIE. **7419** 741909 (2009).
16. J. P. Curran, J. L. Dungan, H. L. Gholz, "Exploring the relationship between reflectance red edge and chlorophyll content in slash pine," Tree Physiol. **7**, 33-48 (1990).
17. A. Gitelson, Y. Gritz, M. Merzlyak, "Relationsihps between leaf chlorophyll content and spectral reflectance and algorithms for non-destructive chlorophyll assessment in higher plant leaves," J. Plant Physiol. **160**, 271-282 (2003).
18. *Landsat 7 Science Data Users Handbook*. NASA, Chapter 8.1.2 "Radiometric Calibration" (2009).

1. Introduction

Multispectral imaging is a valuable technique in remote sensing and biomedical imaging [1, 2]. Several sensing modalities exist for measuring multispectral data. One method time-sequentially images a scene through multiple filters, placed in front of a standard lens and focal plane array (FPA) [3]. This produces a relatively simple and inexpensive instrument. However, since each spectral passband is measured at a different time, error is introduced when viewing temporally dynamic scenes. Consequently, the multispectral passbands must be measured in parallel. For some implementations, these parallel measurements are obtained with multiple cameras, lenses and filters [4]. Another method, which is likely the most common use and implementation of multispectral imaging, can be considered a division of FPA (DoF) approach. In DoF, different filters are placed onto the pixels of a CCD camera, similar to a standard consumer color camera [5]. For application-specific selection of the passbands, "super-pixels" are created that typically contain 2x2 pixels, where each pixel contains a unique spectral passband. This produces a compact 4 band multispectral camera [6].

The method for multispectral imaging, demonstrated here, is derived from a snapshot imaging polarimeter initially developed by K. Oka [7]. Oka's interferometric technique demonstrated that the 2D Stokes parameters can be amplitude modulated onto spatial carrier frequencies. Reconstruction of the 2D state of polarization is accomplished by Fourier filtering each carrier frequency component. This enables snapshot measurement of the complete 2D Stokes vector. However, one drawback of this technique is that long coherence-length (narrow-band) illumination is required. For applications requiring passive illumination, limitations are encountered due to the low signal to noise ratio of the measured data [8]. In an attempt to remedy the narrow-bandwidth limitation, the dispersion-compensated polarization Sagnac interferometer (DCPSI) was developed [9]. Through its mathematical development, it was discovered that a further extension of the carrier frequency technique can be realized. Whereas the original DCPSI amplitude modulates *Stokes parameters* onto carrier frequencies, it is possible, with a minor modification, to modulate *unique spectral passbands* onto carrier frequencies. This device creates a new sensor implementation for snapshot multispectral imaging.

In this paper, we outline the theoretical and experimental development of a multispectral Sagnac interferometer (MSI). In section 2, the theoretical background of a standard polarization Sagnac interferometer (PSI), when used for polarimetric imaging, is outlined to provide a context for the work. In section 3, details regarding the theory of the DCPSI are overviewed. In section 4, the multispectral variant of the DCPSI is introduced, and the key differences between the MSI and DCPSI are explained. Lastly, in section 5, the experimental validation and calibration of the MSI are detailed, followed by a brief conclusion of the work in section 6.

2. Polarization Sagnac interferometer for polarimetric imaging

The multispectral Sagnac interferometer (MSI) is an extension of a standard polarization Sagnac interferometer (PSI) when it is used for Stokes imaging polarimetry [10]. One configuration for a PSI is depicted in Fig. 1.

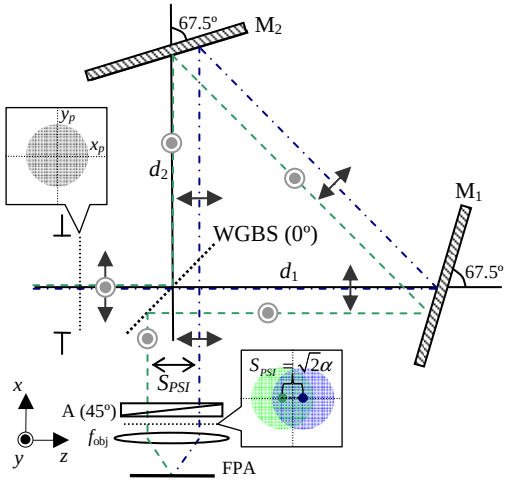

Fig. 1. One configuration for a polarization Sagnac interferometer. The distance between the WGBS and mirrors, M_1 and M_2, is denoted d_1 and d_2, respectively. A shear (S_{PSI}) is produced when $d_1 \neq d_2$. The case $d_1 > d_2$ is illustrated, with $d_1 = d_2 + \alpha$.

The PSI consists of two mirrors, M_1 and M_2, with a wire grid polarization beamsplitter (WGBS), a focal plane array (FPA), and an objective lens with focal length f_{obj}. The WGBS is oriented with its transmission axis at 0° with respect to the x-axis. Two beams, with a shear S_{PSI}, are created when $d_1 \neq d_2$. If the distance, d_1, is offset by an amount α, such that $d_1 = d_2 + \alpha$, the shear is

$$S_{PSI} = \sqrt{2}\alpha \,. \tag{1}$$

Therefore, the shear is directly proportional to the difference in the mirror to WGBS separation. Furthermore, the shear is achromatic; it is independent of the wavelength of the incident illumination.

The functional form of the intensity pattern incident on the FPA can be calculated by considering the optical path difference (OPD). The OPD between the two sheared beams exiting the system is depicted in Fig. 2, and is given by

$$OPD = S_{PSI} \sin(\theta) \approx S_{PSI}\theta \,, \tag{2}$$

where θ is the angle of the incident ray [11]. When the two beams are combined by the lens, they produce interference fringes on the FPA. The interference between the two sheared rays can be expressed as

$$I_{PSI}(x_i, y_i) = \left\langle \left| \frac{1}{\sqrt{2}} E_x(x_i, y_i, t) e^{-j\phi_1} + \frac{1}{\sqrt{2}} E_y(x_i, y_i, t) e^{-j\phi_2} \right|^2 \right\rangle, \tag{3}$$

where < > represents the time average, x_i and y_i are image-plane coordinates, and φ_1, φ_2, are the cumulative phases of each ray. Expansion of this expression yields

$$I_{PSI}(x_i, y_i) = \frac{1}{2}\left\{\begin{array}{l}\left(\left\langle E_x E_x^*\right\rangle + \left\langle E_y E_y^*\right\rangle\right) + \left(\left\langle E_x E_y^*\right\rangle + \left\langle E_x^* E_y\right\rangle\right)\cos(\phi_1 - \phi_2) + \\ j\left(-\left\langle E_x E_y^*\right\rangle + \left\langle E_x^* E_y\right\rangle\right)\sin(\phi_1 - \phi_2)\end{array}\right\}, \quad (4)$$

where E_x, E_y are now implicitly dependent on x_i and y_i. The phase factors are

$$\phi_1 = \frac{2\pi}{\lambda f_{obj}}\frac{\alpha}{\sqrt{2}}x_i \quad \text{and} \quad \phi_2 = -\frac{2\pi}{\lambda f_{obj}}\frac{\alpha}{\sqrt{2}}x_i\,. \quad (5)$$

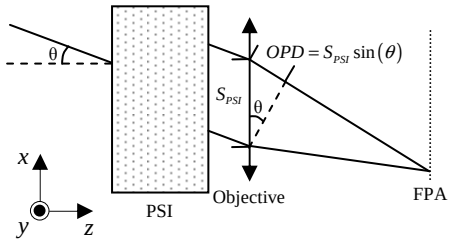

Fig. 2. OPD generated by a shearing distance, S_{PSI}, for a PSI and simplified SPP.

I_{PSI} can be re-expressed in terms of the Stokes parameters. The Stokes parameters are defined from the components of the electric field as [12]

$$\begin{bmatrix} S_0 \\ S_1 \\ S_2 \\ S_3 \end{bmatrix} = \begin{bmatrix} \left\langle E_x E_x^*\right\rangle + \left\langle E_y E_y^*\right\rangle \\ \left\langle E_x E_x^*\right\rangle - \left\langle E_y E_y^*\right\rangle \\ \left\langle E_x E_y^*\right\rangle + \left\langle E_x^* E_y\right\rangle \\ j\left(\left\langle E_x E_y^*\right\rangle - \left\langle E_x^* E_y\right\rangle\right) \end{bmatrix}. \quad (6)$$

Re-expressing Eq. 4 by use of the Stokes parameter definitions and φ_1, φ_2, yields

$$I_{PSI}(x_i, y_i) = \frac{1}{2}\left[S_0 + S_2\cos\left(\frac{2\pi}{\lambda f_{obj}}\sqrt{2}\alpha x_i\right) - S_3\sin\left(\frac{2\pi}{\lambda f_{obj}}\sqrt{2}\alpha x_i\right)\right]. \quad (7)$$

Consequently, the PSI modulates the Stokes parameters S_2 and S_3 onto a carrier frequency, while S_0 remains as an un-modulated component. Fourier filtering can then be utilized to demodulate and reconstruct the spatially dependent Stokes parameters. The spatial carrier frequency modulating the Stokes parameters is

$$U_{PSI} = \frac{\sqrt{2}\alpha}{\lambda f_{obj}}\,. \quad (8)$$

Notable in the carrier frequency is the inverse relationship to the wavelength. Therefore, spectrally narrow-band illumination must be used in order to maintain high carrier frequency visibility across the FPA. This narrow-bandwidth requirement can be disadvantageous with regard to the system's radiometric throughput, thereby decreasing the signal-to-noise ratio of the reconstructed Stokes parameters.

To maintain high fringe visibility over a broad bandwidth (white light), a dispersion compensated polarization Sagnac interferometer (DCPSI) was developed. The DCPSI generates a shear that is linearly proportional to the wavelength, such that $S_{shear} \propto \lambda\gamma$, where γ is an optical thickness, analogous to α.

3. Dispersion compensated polarization Sagnac interferometer (DCPSI)

Compensation of the dispersion in the PSI's carrier frequency can be realized with the introduction of two blazed diffraction gratings [9]. Diffraction gratings are known for their ability to generate white-light interference fringes [13]. The optical layout now takes the form of the dispersion-compensated PSI (DCPSI) depicted in Fig. 3, and is the PSI observed previously in Fig. 1 with $d_1 = d_2$ and the inclusion of two identical gratings, G_1 and G_2. A ray's diffraction angle, after transmission through G_1 or G_2, is calculated for normal incidence by

$$\sin(\theta) = \frac{m\lambda}{d}, \tag{9}$$

where θ is the diffraction angle of the ray as measured from the grating's normal, m is the order of diffraction, and d is the period of the grating. Since d is typically large (> 30 μm), small angle approximations can be used to simplify Eq. 9, yielding $\theta \approx m\lambda/d$.

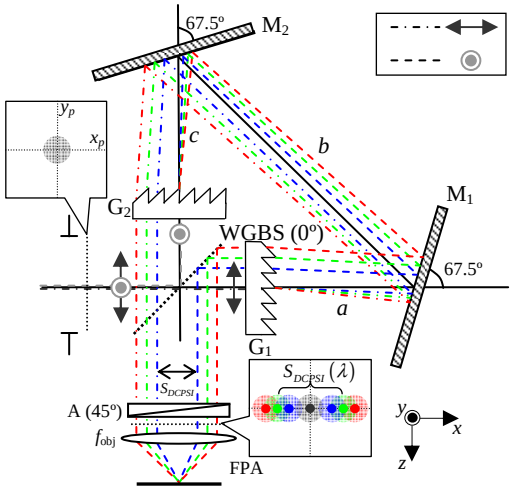

Fig. 3. DCPSI with blazed diffraction gratings, G_1 and G_2, positioned at each output of the WGBS. To remove the achromatic shear, the distance between the WGBS and mirrors, M_1 and M_2, depicted previously in Fig. 1, is $d_1 = d_2$. Inclusion of the gratings generates a shear that is directly proportional to the wavelength.

In the DCPSI, the spectrally broadband beam transmitted by the WGBS is diffracted by G_1 into the +1 order. When these dispersed rays are incident on G_2, the diffraction angle, induced previously by G_1, is removed. The rays emerge parallel to the optical axis, but are offset by a distance proportional to $-\lambda x_o$, where x_o is some constant related to the DCPSI's parameters. Conversely, the beam reflected by the WGBS is initially diffracted by G_2. The dispersed rays are then diffracted to be parallel to the optical axis by G_1, and exit the system offset by a distance proportional to $+\lambda x_o$. Assuming small angles and that G_1 and G_2 are identical, the shear, S_{DCPSI}, is

$$S_{DCPSI} = 2\frac{m\lambda}{d}(a+b+c) \tag{10}$$

where a, b, and c represent the distances between G_1 and M_1, M_1 and M_2, and M_2 and G_2, respectively. Hence, the DCPSI can, to first order, generate a shear that is directly proportional to the wavelength. This makes the phase factors

$$\phi_1 = \frac{2\pi}{f_{obj}}\frac{m}{d}(a+b+c)x_i \quad \text{and} \quad \phi_2 = -\frac{2\pi}{f_{obj}}\frac{m}{d}(a+b+c)x_i \,. \tag{11}$$

Using these phase factors, the intensity on the FPA is

$$I_{DCPSI}(x_i, y_i) = \frac{1}{2}\sum_{m=0}^{d/\lambda_{\min}} S_0^{'}(m) + \frac{1}{2}\sum_{m=1}^{d/\lambda_{\min}} \left[\begin{array}{c} S_2^{'}(m)\cos\left(\frac{2\pi}{f_{obj}}\frac{2m}{d}(a+b+c)x_i\right) \\ -S_3^{'}(m)\sin\left(\frac{2\pi}{f_{obj}}\frac{2m}{d}(a+b+c)x_i\right) \end{array} \right] \tag{12}$$

where the total intensity pattern is a summation from the minimum to maximum order of a blazed grating, such that the maximum order is $(d/\lambda_{\min})\sin(\pi/2)$, where $\lambda_{\min}$ is the minimum wavelength passed by the optical system. $S_0^{'}(m)$, $S_2^{'}(m)$, and $S_3^{'}(m)$ are the Stokes parameters weighted by the diffraction efficiency (DE) of both gratings before integration over wavelength,

$$S_0^{'}(m) = \int_{\lambda_{\min}}^{\lambda_{\max}} DE^2(\lambda, m) S_0(\lambda) d\lambda \tag{13}$$

$$S_2^{'}(m) = \int_{\lambda_{\min}}^{\lambda_{\max}} DE^2(\lambda, m) S_2(\lambda) d\lambda \tag{14}$$

$$S_3^{'}(m) = \int_{\lambda_{\min}}^{\lambda_{\max}} DE^2(\lambda, m) S_3(\lambda) d\lambda \tag{15}$$

where $\lambda_{\min}$ and $\lambda_{\max}$ denote the minimum and maximum wavelengths passed by the optical system. The carrier frequency, U_{DCPSI}, is

$$U_{DCPSI} = \frac{2m}{df_{obj}}(a+b+c) \,. \tag{16}$$

Therefore, insertion of the blazed diffraction gratings enables the dispersion, observed previously in Eq. 8, to be removed from the carrier frequency. Application of the DCPSI towards imaging polarimetry is described in Ref. [9] in which a single-order blazed diffraction grating is utilized. However, the carrier frequency's dependence upon the diffraction order, *m*, can be exploited for multispectral imaging. This is accomplished by substituting the single-order gratings of the DCPSI with multiple-order gratings.

4. Multispectral variant of the DCPSI

The MSI is nearly identical to the DCPSI depicted in Fig. 3, except that the blazed gratings, G_1 and G_2, now have multiple-orders over the sensor's operating bandwidth. The difference between the gratings is depicted in Fig. 4, where the multiple-order structure in Fig. 4 (b) has a taller grove profile than its single-order counterpart, per Fig. 4 (a). The theoretical diffraction efficiency (DE) for an ideal blazed grating is calculated by,

$$DE(\lambda, m) = \mathrm{sinc}^2\left(\frac{m - OPD}{\lambda}\right) \tag{17}$$

with

$$OPD = h\left(n_1 - n_2\right) \tag{18}$$

where h is the grove height and n_1, n_2 are the indices of refraction for the incident and blaze medium, respectively [14].

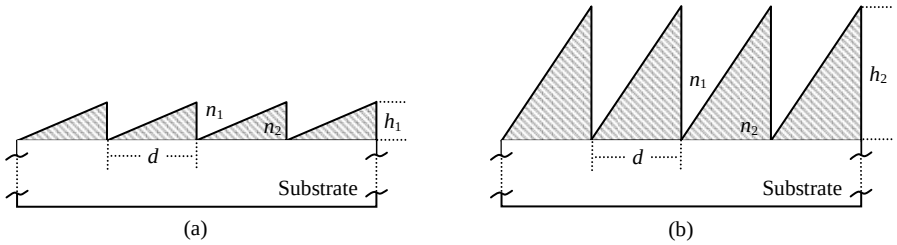

Fig. 4. (a) Single order blazed grating, where d is the period, n_1 and n_2 are the indices of refraction for the incident and blaze medium, respectively, and h_1 is the depth ($OPD \sim 1$ wave). (b) Multiple-order blaze grating, where h_2 is typically 3-10 times larger than h_1.

Using Eq. 17, the theoretical diffraction efficiency for both a single and multiple order blazed grating was calculated. Fig. 5 (a) demonstrates the efficiency assuming a single-order grating with h_1 = 1.28 μm, n_1 = 1.0 and n_2 = 1.5. This yields a first order blaze wavelength of λ_1 = 640 nm, making it the dominant order for wavelengths spanning 425 – 1000 nm. Similarly, Fig. 5 (b) depicts the efficiency for a multiple-order grating with h_2 = 4.07 μm, n_1 = 1.0 and n_2 = 1.5. This produces a first order blaze wavelength of λ_1 = 2035 nm, meaning that the higher orders (m = 2 through 5) are distributed over 400-1000 nm. The blaze wavelength for the higher orders is λ_1/m, such that λ_2 = 1017 nm, λ_3 = 678 nm, λ_4 = 508 nm, and λ_5 = 407 nm.

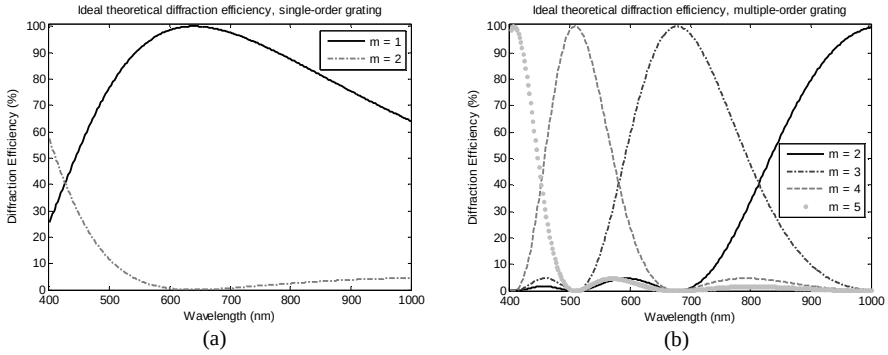

Fig. 5. (a) Diffraction efficiency (percent) for a single order blazed grating in air with h_1 = 1.28 μm and n = 1.5. (b) Multiple order blazed grating in air with h_2 = 4.07 μm and n = 1.5.

As is demonstrated in Fig. 5 (b), use of a multiple-order grating will generate several diffraction orders within the system, where each order has a unique blaze wavelength and spectral passband. Due to the carrier frequency's dependence on the order m, each spectral passband is modulated onto a different spatial carrier frequency. Isolating each passband is accomplished by use of Fourier filtering, detailed in section 5.1.

Besides including the multiple-order gratings, an additional modification is needed to the system (Fig. 3) for measurements of the incident spectral components; namely, a linear polarizer (LP) must be inserted in front of the WGBS. If the LP's transmission axis is oriented at 45° with respect to the x-axis, then the Stokes vector incident on the WGBS is

$$\mathbf{S}_{WGBS} = \frac{1}{2}\begin{bmatrix} 1 & 0 & 1 & 0 \\ 0 & 0 & 0 & 0 \\ 1 & 0 & 1 & 0 \\ 0 & 0 & 0 & 0 \end{bmatrix}\begin{bmatrix} S_0 \\ S_1 \\ S_2 \\ S_3 \end{bmatrix} = \begin{bmatrix} S_0 + S_2 \\ 0 \\ S_0 + S_2 \\ 0 \end{bmatrix}. \quad (19)$$

The intensity pattern for the MSI becomes

$$I_{MSI}(x_i, y_i) = \frac{1}{2}\sum_{m=0}^{\mathrm{Ce}[\lambda_1/\lambda_{\min}]}\left[S_0^{"}(m)\right] + \frac{1}{2}\sum_{m=1}^{\mathrm{Ce}[\lambda_1/\lambda_{\min}]}\left[S_0^{"}(m)\cos\left(\frac{2\pi}{f_{obj}}\frac{2m}{d}(a+b+c)x_i\right)\right], \quad (20)$$

where

$$S_0^{"}(m) = \int_{\lambda_1}^{\lambda_2} DE^2(\lambda, m)\left(S_0(\lambda) + S_2(\lambda)\right)d\lambda. \quad (21)$$

It should be noted that the *dominant* orders experimentally observed in the system correspond to the ceiling (Ce) of $\lambda_1/\lambda_{\min}$, where λ_1 is the first order blaze wavelength of the diffraction grating. This changes the maximum limit of the summation from $d/\lambda_{\min}$ to $\mathrm{Ce}[\lambda_1/\lambda_{\min}]$ in Eq. 20. Furthermore, if S_2 is negligible in Eq. 21, then the modulated information corresponds to the incident S_0 component (*i.e.* the total incident irradiance). Consequently, S_2 in the scene can cause error in the resulting multispectral data. To make the contribution of S_2 negligible, scenes consisted of diffuse surfaces oriented normal to the optical system. Additionally, the illumination source was always oriented to preferentially reflect light in the S_1 state. Further analysis of the error due to this effect is beyond the scope of the current study. However, a design that is effectively polarization insensitive can be made by replacing the WGBS with a standard 50/50 beamsplitter.

5. Experimental verification of the MSI

To verify the operating principles of the MSI, the experimental setup depicted in Fig. 6 was implemented. Spatially and temporally incoherent light is configured by aiming the output of a fiber-light, sourced by a tungsten-halogen lamp, onto a diffuse object. A dichroic polymer linear polarizer at 45° is used to linearly polarize the light, such that the S_0 Stokes parameter can be modulated onto the carrier frequencies (Eq. 19). The WGBS has a clear aperture of 21 mm and consists of anti-reflection coated aluminum wires. Mirrors M_1 and M_2 are 25 mm diameter $1/10^{th}$ wave optical flats. A zoom lens, with focal length f_c = 70-300 mm (F/11), is used to image the object plane to infinity, while an objective lens, with focal length f_{obj} = 250 mm, is used for re-imaging. The diffraction gratings, G_1 and G_2, are blazed for a first order (m = 1) wavelength of λ_1 = 2035 nm on a BK7 substrate with a period d = 69.9 μm. A depiction of the ideal theoretical diffraction efficiencies for these grating parameters was provided previously in Fig. 5 (b). Lastly, an IR blocking filter is used to reject light with wavelengths longer than 750 nm.

Another aspect of the setup involves the placement of an iris, set to a 4 mm diameter, between the zoom lens and WGBS. During initial experimentation, it was observed that the fringe visibility decreased as the aperture diameter increased. Consequently, the optical surface of the WGBS was quantified in a Twyman-Green interferometer to have 3 waves of astigmatism. Therefore, the iris restricts the illuminated area of the WGBS to reduce the effect of this aberration.

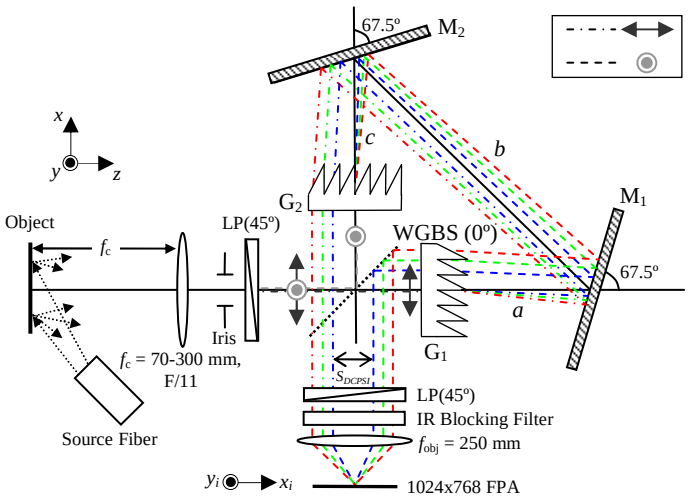

Fig. 6. Experimental setup of the MSI with *a*, *b*, and *c* set to 13.3 mm, 51.4 mm, and 19.1 mm, respectively. An IR blocking filter keeps wavelengths > 750 nm from entering the system.

5.1 MSI calibration

In order to calibrate and reconstruct data from the instrument, data processing is accomplished in the Fourier domain [7]. Taking the Fourier transform of the intensity pattern (Eq. 12) yields

$$\mathfrak{F}\left[I_{MSI}(x_i,y_i)\right]=\frac{1}{2}\sum_{m=0}^{\mathrm{Ce}[\lambda_1/\lambda_{\min}]}\left[S_0^{''}(m)\right]\delta(\xi,\eta)+\sum_{m=1}^{\mathrm{Ce}[\lambda_1/\lambda_{\min}]}\left[S_0^{''}(m)\delta\left(\xi-U_{MSI}(m),\eta\right)\right]+\sum_{m=1}^{\mathrm{Ce}[\lambda_1/\lambda_{\min}]}\left[S_0^{''}(m)\delta\left(\xi+U_{MSI}(m),\eta\right)\right] \tag{22}$$

with

$$U_{MSI}(m)=\frac{2m}{df_{obj}}(a+b+c), \tag{23}$$

where δ is the Dirac-delta function and ξ, η are the Fourier transform variables along x_i and y_i, respectively. Extraction of the Stokes parameters is accomplished by taking an inverse Fourier transform of the filtered carrier frequencies, or "channels." Filtration and inverse Fourier transformation of the $\delta(\xi,\eta)$ (channel C_0) and $\delta\left(\xi+U_{MSI}(m),\eta\right)$ (channel $C_1(m)$) components yields

$$\mathfrak{F}^{-1}[C_0]=\frac{1}{2}\sum_{m=0}^{\mathrm{Ce}[\lambda_1/\lambda_{\min}]}S_0^{''}(m) \tag{24}$$

$$\mathfrak{F}^{-1}\left[C_1(m)\right]=\frac{1}{4}S_0^{''}(m)\exp\left(j2\pi U_{MSI}(m)x_i\right). \tag{25}$$

Extraction of the spectral passbands, $S_0^{''}(m)$, requires demodulation of the exponential phase factor. Since knowledge of the phase is irrelevant for reconstruction ($S_0^{''}$ is always positive), demodulation is achieved by taking the absolute value of the filtered channel,

$$\left|\mathfrak{F}^{-1}\left[C_1(m)\right]\right|=\frac{1}{4}S_0^{''}(m). \tag{26}$$

A 150x150 pixel section, from a raw image of a uniformly illuminated high reflectance diffuser, is depicted in Fig. 7 (a). The Fourier transformation of the image is depicted in Fig. 7 (b), demonstrating the presence of a center-burst and four carrier frequencies, along with their conjugates.

Notable is that the image and Fourier domain is rotated by approximately 31º. This rotation was induced by rotating the camera to reduce reconstruction artifacts caused by aliasing between adjacent channels [15]. Specifically, it reduces aliasing caused by the large side-lobes of the carrier frequency components along ξ' and η', originating from the nature of the 2D *sinc* function. Further discussion of error related to this phenomenon is beyond the scope of the current paper. However, it should be mentioned that while changing the shearing direction (*i.e.* rotating the gratings) will rotate the fringes without rotating the image, doing so was not feasible in our experimental setup due to optomechanical limitations.

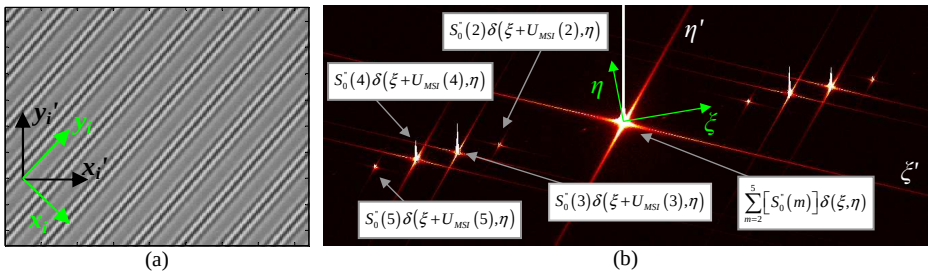

(a) (b)

Fig. 7. (a) Raw image of a uniformly illuminated diffuser demonstrating the fringe pattern in the MSI. (b) Fourier transformation of the raw image data in (a). Four carrier frequencies are observed, corresponding to m = 2, 3, 4 and 5.

5.2 Spectral passbands

The operating principles discussed previously indicate that the order-dependent carrier frequencies are visible only when the sensor is illuminated with light at specific wavelengths. To validate that the passbands correspond to a given diffraction order and to measure their relative spectral responsivity, the experimental setup depicted in Fig. 8 was implemented. A monochrometer, sourced by a tungsten halogen lamp, is used to generate narrowband light. The exit slit of the monochrometer was then imaged by the MSI. Using a focal length of 70 mm for the collimating lens ensured that the edges of the slit were not visible, such that fringes were present across the entire FOV.

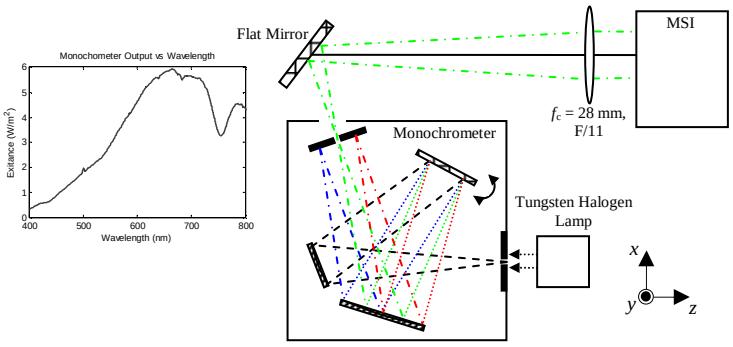

Fig. 8. Monochrometer configuration for sending light into the MSI for verification of the fringe visibility. The bandwidth of the light exiting the monochrometer was approximately 10.5 nm using a 3 mm exit slit.

To calculate the relative responsivity, a calibrated spectrometer was used to characterize the output of the monochrometer. For radiometric calibration of the spectrometer, a NIST-

traceable tungsten halogen lamp was utilized. This enabled the output of the monochrometer to be characterized in radiometric units, as illustrated in Fig. 9 (Left). The response of each channel was then measured by Eq. 26 as the monochrometer was scanned from 400-800 nm in 10 nm increments. An average of approximately 100x100 pixels from the center of the image was then calculated and normalized by the measured response of the monochrometer. The relative response for each channel is depicted in Fig. 9 (Right) alongside the combined relative response of the FPA and IR blocking filter; the response of the other optical elements in the system (dichroic linear polarizers, lenses, beamsplitter, etc.) is not included in this curve. Despite this, the relative spectral response of each channel generally follows the trends of the FPA and filter.

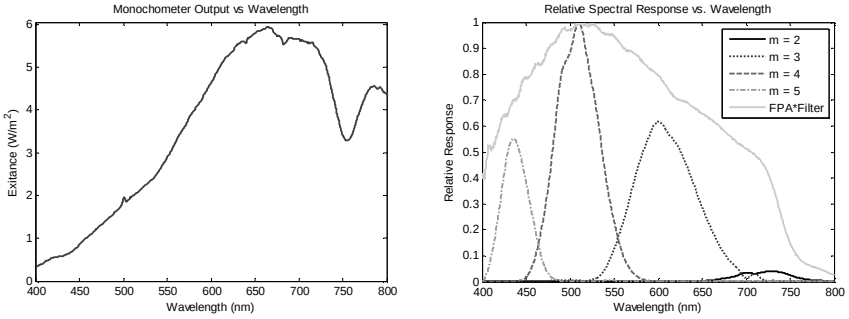

Fig. 9. (Left) Measured monochrometer output, proportional to W/m^2. (Right) Measured relative spectral response of the different passbands within the MSI. Also included (solid light-gray line) is the relative response of the FPA multiplied by the measured transmission of the IR blocking filter.

5.3 Multispectral reconstruction validation

To validate the accuracy of the multispectral reconstructions from the MSI, experiments were performed that compared MSI results to that of the calibrated spectrometer (U2S). Specifically, reflectance measurements of a healthy and unhealthy tree leaf, taken from an *Acacia crassifolia*, were measured with the MSI and the U2S. These samples enabled the characteristic reflectance features of chlorophyll, which is present in the healthy leaf but largely absent in the unhealthy leaf, to be used for the comparison [16, 17]. Reflectance measurements from the U2S were matched to the MSI's passbands by

$$R_{\mathrm{U2S}}(m) = \frac{\int_{400}^{800} I_{leaf}(\lambda) T_{MSI}(m,\lambda)\, d\lambda}{\int_{400}^{800} I_{diffuser}(\lambda) T_{MSI}(m,\lambda)\, d\lambda}, \tag{27}$$

where λ is the wavelength in nm, T_{MSI} is the relative response of the passband of order m per Fig. 9, and I_{leaf}, $I_{diffuser}$ is the measured irradiance of the leaf and of a white diffuse reflectance panel, respectively. The reflectance measurement from the MSI is calculated by

$$R_{MSIavg}(m) = \frac{\sum_{l}\sum_{n} I_{leaf}(l,n,m)}{\sum_{l}\sum_{n} I_{diffuser}(l,n,m)}, \tag{28}$$

where l and n are integers representing pixels in x and y, respectively. Here, the inner 90% of the image is used in the summation to average over a large area (~25 mm^2) of the sample.

The two experimental configurations for the reflectance measurements are depicted in Fig. 10, where the source and viewing geometry between both the U2S and MSI is maintained for both measurements. Since the U2S is non-imaging, defocus was implemented in the MSI to obtain reflectance measurements that average over the observed area of the sample.

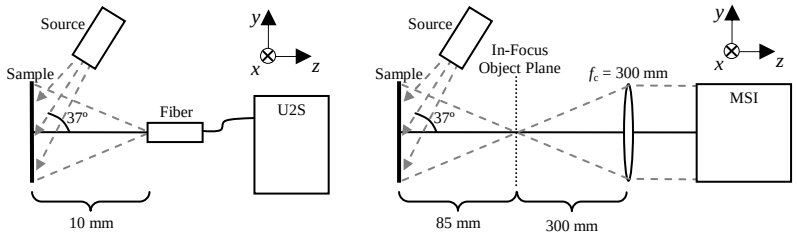

Fig. 10. (Left) System setup for U2S reflectance measurements. The incidence angle of the source (tungsten-halogen lamp) was approximately 37º with respect to the surface normal of the sample. (Right) System setup for MSI reflectance measurements. The sample is defocused to average the reflectance over the observed area.

The measured reflectance from the U2S and the MSI yields the results portrayed in Fig. 11.

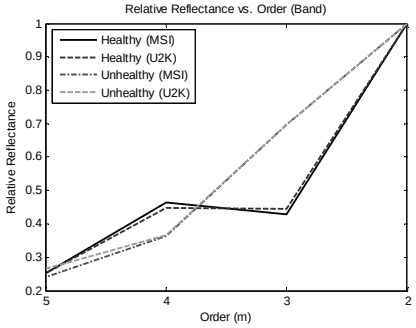

Fig. 11. Relative reflectance of the healthy and unhealthy leaves, normalized to the irradiance in order 2, as measured with the MSI and U2S. The healthy vegetation experiences more absorption in order 3 due to the presence of chlorophyll.

The root mean square (RMS) error between the MSI and U2S data is calculated with

$$\varepsilon = \sqrt{\frac{1}{4}\sum_{m=2}^{5}\left(R_{\mathrm{U2S}}(m) - R_{MSI}(m)\right)^2}\,. \tag{29}$$

The RMS error for the healthy and unhealthy leaf samples yields 0.0115 and 0.0117, respectively. Consequently, the error in the spectral reconstruction is on the order of 1.2 percent between the U2S and the MSI.

5.4 Multispectral spatial reconstructions

To demonstrate the in focus imaging capabilities of the MSI, both the healthy and unhealthy leaf samples were imaged simultaneously with the sensor. A relative reflectance calculation was performed using

$$R_{MSI}(l,n,m) = \frac{I_{leaf}(l,n,m)}{I_{diffuser}(l,n,m)}\,. \tag{30}$$

The band-integrated image, taken by demodulating the first component in Eq. 22, is depicted in Fig. 12 (a), while an image from each band (or order) is depicted in the bottom row. An

additional calculation, demonstrating the applicability of the results, is the normalized difference vegetation index (NDVI) provided in Fig. 12 (b). The NDVI is calculated by

$$NDVI(l,n) = \frac{I(l,n,2) - I(l,n,3)}{I(l,n,2) + I(l,n,3)}, \tag{31}$$

If the leaf has a high chlorophyll content, order 3 will contain less reflected energy than order 2, yielding a high NDVI. Conversely, if the leaf has little to no chlorophyll, order 3 will have nearly equal reflected energy compared to order 2, yielding a low NDVI. This is observed in the NDVI image, where the upper left portion of the scene (quadrant 2) contains the unhealthy leaf, while the lower right region (quadrant 4) contains the healthy leaf.

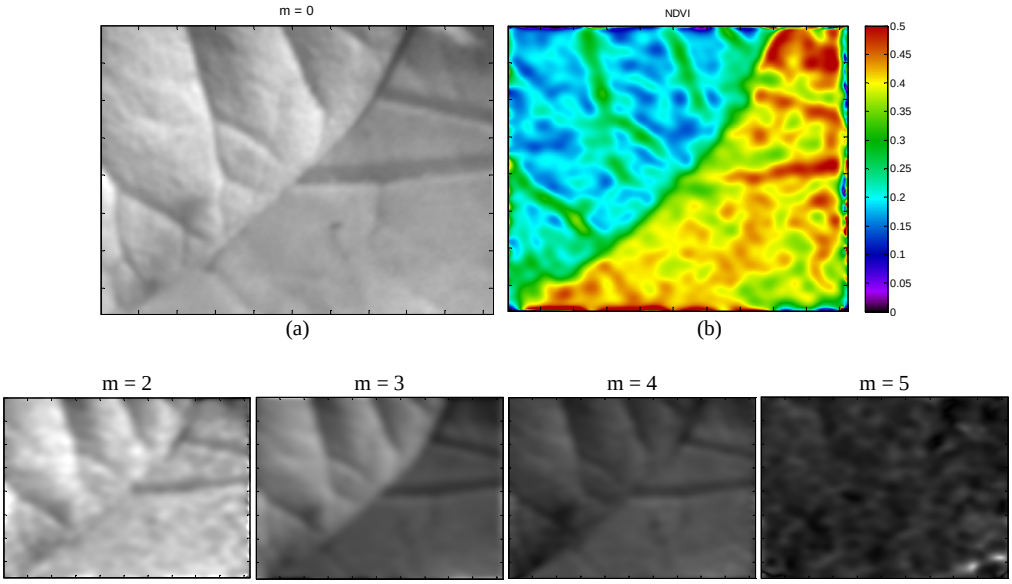

Fig. 12. Relative reflectance images of a healthy and unhealthy leaf. (a) Band-integrated image. (b) normalized difference vegetation index (NDVI). (Bottom) Image from each order (m = 2 through m = 5).

Since the near infrared (NIR) band (order 2) spans wavelengths from 685-755 nm full width half-max, order 2 integrates across the vegetative red edge. Consequently, the NDVI calculation performed here is more analogous to the calculation performed in Ref. [17]. Gitelson demonstrates that an NDVI calculation performed between two bands, located at 525-555 nm and 695-705 nm, can be linearly related to the vegetation's chlorophyll concentration. This is in opposition to an NDVI calculation performed with Landsat 7's band 4 (780-900 nm) with ETM+ [18]. The MSI and Landsat 7 NIR band is overlaid onto the measured relative reflectance for *Acacia crassifolia* per Fig. 13. Ultimately, the system can be designed to incorporate the appropriate bands to perform an NDVI measurement analogous to Landsat 7, or other passbands given the requirements of a specific application.

Application of the MSI's multispectral imaging capabilities is further illustrated in outdoor test results. A photo of an outdoor scene, taken with a color digital camera, is depicted in Fig. 14. The reconstructed spectrally band-integrated image from the MSI is depicted in Fig. 15 (a), while an image from each band is depicted in the bottom row. The NDVI image is portrayed in Fig. 15 (b). This demonstrates the sensor's ability to operate in a remote sensing capacity.

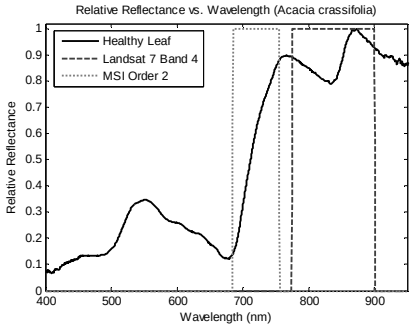

Fig. 13. Relative reflectance of a healthy leaf from *Acacia crassifolia* measured with the U2S (solid black line). The "red edge" begins at 700 nm and peaks at approximately 765 nm. The Landsat 7 (band 4) spans 775-900 nm (dark dashed line) while the MSI spans 685-755 nm (gray dotted line).

Fig. 14. Photo taken with a standard color digital camera of an outdoor scene. Healthy vegetation is present, in addition to brick, concrete, and a relatively clear sky.

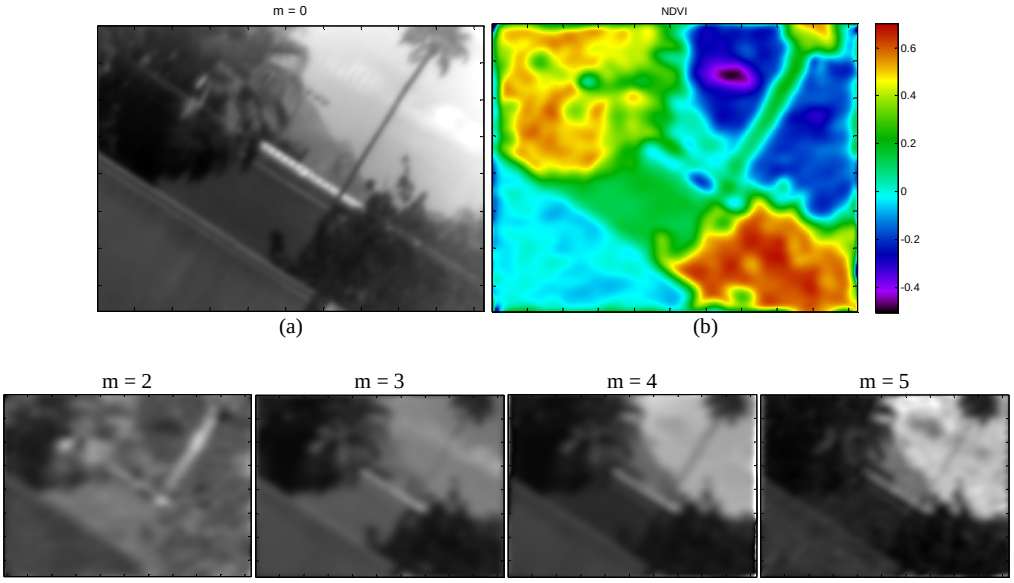

Fig. 15. Relative reflectance images of an outdoor scene. (a) Band-integrated image. (b) normalized difference vegetation index (NDVI). (Bottom) Image from each order (m = 2 through m = 5).

6. Conclusion

The development, calibration, validation and experimental results of a different kind of multispectral imager have been presented. The multispectral Sagnac interferometer (MSI) was created by modifying the dispersion compensated polarization Sagnac interferometer (DCPSI) originally used for snapshot polarimetric imaging. By replacing the single-order blazed diffraction gratings with multiple-order gratings, each diffraction order's distinctive spectral response is encoded onto unique spatial carrier frequencies. The multispectral reconstruction's RMS error, as calculated between the MSI and a calibrated spectrometer, was measured to be approximately 1.2 percent for both a healthy and unhealthy leaf from *Acacia crassifolia*. The imaging potential of the MSI was demonstrated through NDVI measurements of the same leaf samples, in addition to outdoor measurements of scenes containing vegetation. Ultimately, the sensor compromises spatial resolution to capture the spectral components. However, it is envisioned that, with further optimization, the spatial and spectral resolution can be maximized.